Inorg. Chem. **2005**, *44*, 4485–4498

Synthesis, Characterization, and Physicochemical Properties of Manganese(III) and Manganese(V)–Oxo Corrolazines

David E. Lansky,[†] Beaven Mandimutsira,[†] Bobby Ramdhanie,[†] Maria Clausén,[§] James Penner-Hahn,[§] S. A. Zvyagin,[‡] Joshua Telser,[¶] J. Krzystek,[‡] Riqiang Zhan,[||] Zhongping Ou,[||] Karl M. Kadish,*[,||] Lev Zakharov,[⊥] Arnold L. Rheingold,[⊥] and David P. Goldberg*[,†]

Department of Chemistry, Johns Hopkins University, 3400 North Charles Street, Baltimore, Maryland 21218, Department of Chemistry, University of Michigan, Ann Arbor, Michigan 48109, Department of Chemistry and Biochemistry, University of California, San Diego, 9500 Gilman Drive, La Jolla, California 92093, National High Magnetic Field Laboratory, Florida State University, Tallahassee, Florida 32310, Chemistry Program, Roosevelt University, Chicago, Illinois 60605, and Department of Chemistry, University of Houston, Houston, Texas 77204-5003

Received March 9, 2005

The structural and physicochemical properties of the manganese–corrolazine (Cz) complexes (TBP_8Cz)$Mn^{V}{\equiv}O$ (**1**) and (TBP_8Cz)Mn^{III} (**2**) (TBP = *p-tert*-butylphenyl) have been determined. Recrystallization of **2** from toluene/MeOH resulted in the crystal structure of (TBP_8Cz)$Mn^{III}(CH_3OH)$ (**2**·MeOH). The packing diagram of **2**·MeOH reveals hydrogen bonds between MeOH axial ligands and meso N atoms of adjacent molecules. Solution binding studies of **2** with different axial ligands (Cl^-, Et_3PO, and Ph_3PO) reveal strong binding, corroborating the preference of the Mn^{III} ion for a five-coordinate environment. High-frequency and field electron paramagnetic resonance (HFEPR) spectroscopy of solid **2**·MeOH shows that **2**·MeOH is best described as a high-spin ($S = 2$) Mn^{III} complex with zero-field splitting parameters typical of corroles. Structural information on **1** was obtained through an X-ray absorption near-edge structure (XANES)/extended X-ray absorption fine structure (EXAFS) study and compared to XANES/EXAFS data for **2**·MeOH. The XANES data for **1** shows an intense pre-edge transition characteristic of a high-valent metal–oxo species, and a best fit of the EXAFS data gives a short Mn–O bond distance of 1.56 Å, confirming the structure of the metal–oxo unit in **1**. Detailed spectroelectrochemical studies of **1** and **2** were performed revealing multiple reversible redox processes for both complexes, including a relatively low potential for the $Mn^{V} \rightarrow Mn^{IV}$ process in **1** (near 0.0 V vs saturated calomel reference electrode). Chemical reduction of **1** results in the formation of a $Mn^{III}Mn^{IV}(\mu\text{-O})$ dimer as characterized by electron paramagnetic resonance spectroscopy.

Introduction

Interest in synthetic porphyrins and analogous porphyrinoid species stems from their many applications in catalysis and materials and medicinal chemistry and from their use as models for biological systems. Corrolazines,[1−7] and their related corroles,[7−11] are porphyrinoid compounds in which one of the meso atoms has been deleted and replaced with a direct pyrrole−pyrrole bond. The remaining three meso

* To whom correspondence should be addressed. E-mail: dpg@jhu.edu. (D.P.G.); kkadish@uh.edu (K.M.K.).
[†] Johns Hopkins University.
[§] University of Michigan.
[⊥] University of California, San Diego.
[‡] Florida State University.
[¶] Roosevelt University.
[||] University of Houston.

(1) Ramdhanie, B.; Stern, C. L.; Goldberg, D. P. *J. Am. Chem. Soc.* **2001**, *123*, 9447−9448.
(2) Ramdhanie, B.; Zakharov, L. N.; Rheingold, A. L.; Goldberg, D. P. *Inorg. Chem.* **2002**, *41*, 4105−4107.
(3) Mandimutsira, B. S.; Ramdhanie, B.; Todd, R. C.; Wang, H. L.; Zareba, A. A.; Czernuszewicz, R. S.; Goldberg, D. P. *J. Am. Chem. Soc.* **2002**, *124*, 15170−15171.
(4) Wang, S. H. L.; Mandimutsira, B. S.; Todd, R.; Ramdhanie, B.; Fox, J. P.; Goldberg, D. P. *J. Am. Chem. Soc.* **2004**, *126*, 18−19.
(5) Ramdhanie, B.; Telser, J.; Caneschi, A.; Zakharov, L. N.; Rheingold, A. L.; Goldberg, D. P. *J. Am. Chem. Soc.* **2004**, *126*, 2515−2525.
(6) Fox, J. P.; Ramdhanie, B.; Zareba, A. A.; Czernuszewicz, R. S.; Goldberg, D. P. *Inorg. Chem.* **2004**, *43*, 6600−6608.
(7) Gryko, D. T.; Fox, J. P.; Goldberg, D. P. *J. Porphyrins Phthalocyanines* **2004**, *8*, 1091−1105.
(8) Gryko, D. T. *Eur. J. Org. Chem.* **2002**, 1735−1743.
(9) Gross, Z. *JBIC, J. Biol. Inorg. Chem.* **2001**, *6*, 733−738.

10.1021/ic0503636 CCC: $30.25
Published on Web 05/24/2005

positions are occupied by carbon atoms in the case of corroles and nitrogen atoms in the case of corrolazines. Corroles have been the focus of significant synthetic efforts in recent years, which has led to the discovery of facile synthetic methods that have made corroles and their metal complexes more accessible.[8,12−15] Corrolazines, which are new entries in the general corrole family, are also easy to prepare, and the first example of a corrolazine was synthesized by some of us a few years ago.[1] Corroles and corrolazines exhibit physicochemical properties and reactivity patterns that resemble, but are distinctly different from, porphyrins and other porphyrin analogues. Determining these properties for corroles and corrolazines should provide insight into the physicochemical and reactivity properties of porphyrins in general, including their biological counterparts in heme-containing enzymes and proteins.

In a previous paper we reported the synthesis of a manganese(V)−oxo corrolazine, $(TBP_8Cz)Mn^{V}{\equiv}O$ (TBP = *p*-*tert*-butylphenyl; Cz = corrolazine), (**1**).[3] This compound, which was found to be stable at room temperature, was characterized by a variety of spectroscopic techniques, but no direct structural information from X-ray studies were reported. High-valent metal−oxo porphyrinoid compounds are of particular importance because of their putative roles in catalysis[16,17] and heme enzyme mechanisms.[18,19] In particular, high-valent iron−oxo species are implicated as intermediates in synthetic and biological porphyrin-mediated oxidations, such as in cytochrome P450.[20,21] In related studies, manganese porphyrins have been examined as catalysts for P450-type transformations (epoxidation, hydroxylation, N-dealkylation), and a high-valent manganese−oxo porphyrin intermediate is usually invoked.[22−25] Mechanistic proposals for the water oxidation process in photosynthesis have also included putative $Mn^{V}{\equiv}O$ species as intermediates.[26−28] In many of these earlier studies, a high-valent metal−oxo porphyrin species is not observed directly but is invoked from indirect evidence. In this regard, the isolation, direct characterization, and spectroscopic properties of **1** are of interest. In addition, our earlier report described the synthesis of a manganese(III)−corrolazine complex, which was formulated as the four-coordinate $[(TBP_8Cz)Mn^{III}]$ (**2**). This compound was spectroscopically characterized by UV−vis and fast atom bombardment mass spectrometry (FAB-MS), but its structure and other physical properties were not described. Although a four-coordinate environment for Mn^{III} is rare, it was observed in manganese(III) corroles,[29] and thus we wanted to better define the structure and axial ligand preferences of **2**.

In this work, further spectroscopic measurements on **1** and **2** are described with the goal of unambiguously assigning their structures as well as determining in detail several of their physicochemical properties, which have implications for their stability and reactivity. A complete structural characterization of **2** by single-crystal X-ray diffraction has been carried out, and the axial ligand binding properties of **2** have also been investigated. Although X-ray quality single crystals of **1** have thus far eluded preparation, direct structural analysis of **1** has been obtained through an X-ray absorption near-edge structure (XANES)/extended X-ray absorption fine structure (EXAFS) study. High-field electron paramagnetic resonance (HFEPR) spectroscopy has been employed to conclusively assign both the spin and the oxidation states of the Mn ion in **2** and to better understand the ligand field induced by the corrolazine macrocycle. The electrochemical and spectroelectrochemical behaviors of both **1** and **2** have been determined to define the general redox behavior of these Mn corrolazines and compare their behavior with that of Mn corroles. In addition, these measurements provide insight into the ability of corrolazines to stabilize high-valent species such as **1**, which is an important feature of corroles in general.

Experimental Section

General Methods and Instrumentation. The starting material octa-*tert*-butylphenyl corrolazine $[(TBP_8Cz)H_3]$ was synthesized according to published procedures.[1] The manganese(V)−oxo complex **1** appeared to be stable to air, light, and moisture in the solid state, but in solution it was handled under air-free conditions as a precaution. The manganese(III) complex **2** was, in general, stable to air, light, and moisture, and no special precautions were necessary in its handling. Tetrahydrofuran was distilled from sodium/benzophenone, and pyridine was distilled from CaH_2. Other solvents and reagents were of reagent-grade quality and used as received from commercial sources. NMR spectra were recorded on a Varian Unity FT-NMR instrument at 400 MHz (^1H). All spectra were recorded in 5-mm o.d. NMR tubes, and chemical shifts were reported as δ values from standard solvent peaks. Fourier

(10) Erben, C.; Will, S.; Kadish, K. M. In *The Porphyrin Handbook*; Kadish, K. M., Smith, K. M., Guilard, R., Eds.; Academic Press: New York, 2000; Vol. 2, pp 233−300.
(11) Sessler, J. L.; Weghorn, S. J. *Expanded, Contracted, & Isomeric Porphyrins*; Elsevier Science Inc.: New York, 1997; Vol. 15.
(12) Collman, J. P.; Decréau, R. A. *Tetrahedron Lett.* **2003**, *44*, 1207−1210.
(13) Paolesse, R.; Jaquinod, L.; Nurco, D. J.; Mini, S.; Sagone, F.; Boschi, T.; Smith, K. M. *Chem. Commun.* **1999**, 1307−1308.
(14) Gross, Z.; Galili, N.; Saltsman, I. *Angew. Chem., Int. Ed.* **1999**, *38*, 1427−1429.
(15) Guilard, R.; Barbe, J. M.; Stern, C.; Kadish, K. M. In *The Porphyrin Handbook*; Kadish, K. M., Smith, K. M., Guilard, R., Eds.; Elsevier: San Diego, CA, 2003; Vol. 18, pp 303−349.
(16) Sheldon, R. A. *Metalloporphyrins in Catalytic Oxidations*; Marcel Dekker: New York, 1994.
(17) Sheldon, R. A.; Kochi, J. K. *Metal-Catalyzed Oxidations of Organic Compounds*; Academic Press: New York, 1981.
(18) Collman, J. P.; Boulatov, R.; Sunderland, C. J.; Fu, L. *Chem. Rev.* **2004**, *104*, 561−588.
(19) English, A. M.; Tsaprailis, G. *Adv. Inorg. Chem.* **1995**, *43*, 79−125.
(20) Meunier, B.; de Visser, S. P.; Shaik, S. *Chem. Rev.* **2004**, *104*, 3947−3980.
(21) Ortiz de Montellano, P. R.; De Voss, J. J. *Nat. Prod. Rep.* **2002**, *19*, 477−493.
(22) McLain, J. L.; Lee, J.; Groves, J. T. In *Biomimetic Oxidations Catalyzed by Transition Metal Complexes*; Meunier, B., Ed.; Imperial College Press: London, 2000; pp 91−169.
(23) Jin, N.; Bourassa, J. L.; Tizio, S. C.; Groves, J. T. *Angew. Chem., Int. Ed.* **2000**, *39*, 3849−3851.
(24) Jin, N.; Groves, J. T. *J. Am. Chem. Soc.* **1999**, *121*, 2923−2924.
(25) Groves, J. T.; Lee, J.; Marla, S. S. *J. Am. Chem. Soc.* **1997**, *119*, 6269−6273.
(26) Carrell, T. G.; Tyryshkin, A. M.; Dismukes, G. C. *JBIC, J. Biol. Inorg. Chem.* **2002**, *7*, 2−22.
(27) Pecoraro, V. L.; Hsieh, W.-Y. In *Manganese and Its Role in Biological Processes*; Sigel, A., Sigel, H., Eds.; Marcel Dekker: New York, 2000; Vol. 37, pp 429−504.
(28) Hoganson, C. W.; Babcock, G. T. *Science* **1997**, *277*, 1953−1956.
(29) Licoccia, S.; Morgante, E.; Paolesse, R.; Polizio, F.; Senge, M. O.; Tondello, E.; Boschi, T. *Inorg. Chem.* **1997**, *36*, 1564−1570.

transform infrared (FT-IR) spectra were recorded on a Perkin−Elmer RX I FT-IR spectrometer. Electron paramagetic resonance (EPR) spectra were obtained on a Bruker EMX EPR spectrometer controlled with a Bruker ER 041 X G microwave bridge. The EPR spectrometer was equipped with an Oxford Instruments continuous-flow liquid helium cryostat and an ITC503 temperature controller. We simulated X-band EPR spectra using the program DDPOWH3 by Telser. UV−vis spectral studies were performed with an Agilent 8453 diode array spectrometer equipped with HPChemstation software and with a Varian Cary Bio 50 UV−vis spectrophotometer. We obtained mass spectrometry data using a Kratos SEQ MALDI-TOF mass spectrometer. Elemental analyses were performed by Desert Analytics, Tucson, AZ.

[(TBP$_8$Cz)Mn^{III}] (2). The initial synthesis of **2** involved the addition of $Mn^{III}(acac)_3$ (acac = acetylacetonate) to the metal-free corrolazine [(TBP$_8$Cz)H$_3$] in pyridine under high-temperature conditions.[3] Since that first report, we have found an alternative, low-temperature procedure that gives comparable yields of **2**, which is as follows: an amount of $Mn^{III}(acac)_3$ (0.257 g, 0.738 mmol) was added to [(TBP$_8$Cz)H$_3$] (0.100 g, 0.0738 mmol) in CH_2Cl_2/CH_3OH (90:10 v:v). The reaction mixture was allowed to stir at room temperature for 18 h, after which time the solvents were removed on a rotary evaporator to give a dark blue solid. The crude product was purified by chromatography (CH_2Cl_2/CH_3OH) (99:1 v:v; silica gel) to give **2** as a dark green-brown solid (0.098 g, 95%). Crystals suitable for X-ray crystallography were grown from the slow vapor diffusion of MeOH into a solution of **2** in toluene. These crystals were also used for elemental analysis. R_f = 0.88, CH_2Cl_2/MeOH (99:1) on silica gel. UV−vis (CH_2Cl_2): λ_{max}, nm ($\epsilon \times 10^{-4}$ M^{-1} cm^{-1}): 435 (5.85), 562 (1.23), 634 (1.46), 685 (3.49). FAB-MS (*m*/*z*) (NBA matrix): isotopic cluster centered at 1411.4 (M^+), 1434.4 (M + Na, w/ NaI added to the NBA matrix). ^{1}H NMR (400 MHz, CD_2Cl_2): δ (ppm) 12.89 (br), 9.25 (br), 7.13 (br), 1.62 (br); FT-IR (thin film) (cm^{-1}) 2961 vs, 2868 m, 1735 w, 1655 w, 1460 m, 1394 w, 1363 m, 1268 m, 1200 w, 1162 m, 1106 s, 1016 m, 999 vs, 864 w, 835 m. Anal. Calcd for $C_{97}H_{108}N_7MnO$ (**2**·CH_3OH): C, 80.74; H, 7.54; N, 6.79. Found: C, 80.56; H, 7.32; N, 6.79.

[(TBP$_8$Cz)Mn^{V}(O)] (1). In a previous report, **1** was synthesized by the addition of *meta*-chloroperbenzoic acid (mCPBA) to **2** in CH_2Cl_2.[3] An alternative method in which the oxidant has been changed to iodosylbenzene (PhIO) has been developed to avoid difficulties encountered from overoxidation by mCPBA. Excess PhIO (0.763 g, 3.471 mmol) was added to a solution of **2** (0.50 g, 0.347 mmol) in CH_2Cl_2 (25 mL), and the reaction mixture was stirred at room temperature for 30 min. PhIO is only sparingly soluble in CH_2Cl_2, and thus an excess was added to ensure the complete oxidation of **2**. The solution changed from a dark green-brown to a deep green color. The reaction was monitored by UV−vis spectroscopy to confirm the complete conversion of **2** to **1**. The solvent was then removed on a rotary evaporator, and the residue was purified by column chromatography (CH_2Cl_2, silica gel) to give **1** as a dark green solid. Any unreacted PhIO, which is mostly insoluble, was easily removed by the column purification of **1**. The complex **1** is diamagnetic, and its ^{1}H NMR spectrum and other analytical data have been previously reported.[3]

X-ray Crystallography. Crystal data for **2**·$(CH_3OH)(C_7H_8)_3$ at 173(2) K: $C_{118}H_{132}MnN_7O$, M_r = 1719.25, monoclinic, *C*2/*c*, *a* = 39.253(3) Å, *b* = 21.6263(18) Å, *c* = 25.784(2) Å, β = 113.556(2)°, *V* = 20064(3) Å^3, *Z* = 8, ρ = 1.138 g cm^{-3}, *F*(000) = 7376, and μ(Mo Kα) = 0.185 mm^{-1}. X-ray diffraction intensities were collected on a Bruker SMART APEX CCD diffractometer [*T* = 173(2) K, Mo Kα radiation (λ = 0.71073 Å), crystal dimensions: 0.50 × 0.20 × 0.10 mm^{-3}, $2\theta_{max}$ = 56.6°, total number of reflections = 64340, independent reflections = 23476 (R_{int} = 0.0568)]. The structure was solved by direct methods, completed by subsequent difference Fourier syntheses, and refined by full matrix least-squares procedures on F^2. All non-hydrogen atoms were refined with anisotropic displacement coefficients except the disordered carbon atoms of one phenyl ring in the main molecule **2** and the solvent toluene molecules that were refined with isotropic thermal parameters. In the crystal structure, there were three toluene solvent molecules that were refined as riding groups. The H atoms were placed at calculated positions and refined in a riding group model. The number of refinement parameters is 1004. The relatively large thermal parameters of solvent toluene molecules and the carbon atoms of the methyl groups in **2** indicate significant flexibility of the methyl groups and solvent molecules in the crystal structure. The final R factors [$I > 2\sigma(I)$]: R1 = 0.1125, wR2 = 0.3224, GOF = 1.169. All software and sources of the scattering factors are contained in the SHELXTL (5.10) program package (G. Sheldrick, Bruker XRD, Madison, WI).

Binding Studies. The addition of axial ligands to **2** was performed in a 250-mL Schlenk flask that was specially modified to contain a 1-cm path-length quartz cell (total volume = 3 mL) fused to a sidearm assembly, which could then be filled by tilting the flask and allowing the solution to drain from the quartz cell into the sidearm attachment. This setup allowed for the convenient addition of aliquots of stock solutions of the axial ligands (Cl^-, Et_3PO, Ph_3PO) to **2**. A typical experiment involving the addition of Cl^- is as follows: complex **2** was dissolved in CH_2Cl_2 to give a 3.3 μM solution. A stock solution of tetraethylammonium chloride (Et_4NCl) in CH_2Cl_2 (0.33 μM) was added in successive aliquots (0−1.3 equiv) by syringe to the solution of **2** until no further change was observed in the UV−vis spectrum. The titrations were performed at different fixed concentrations of **2** to confirm that the binding constants were not dependent on the concentration of **2**.

A general equilibrium expression is given in eq 1, along with a definition of the binding constant in eq 2.

$$(TBP_8Cz)Mn + L \rightleftharpoons (TBP_8Cz)Mn(L) \quad (1)$$

$$K_a = [(TBP_8Cz)Mn(L)]/\{[(TBP_8Cz)Mn][L]\} \quad (2)$$

An analytical expression for relating the concentration of the bound complex to the amount of ligand added for a 1:1 binding event can be derived from eq 2 by using mass balance relationships and is given in eq 3

$$[(TBP_8Cz)Mn(L)] = [\{[L]_0 + [Mn]_0 + (1/K_a)\} + (\{[L]_0 + [Mn]_0 + (1/K_a)\}^2 - 4[Mn]_0[L]_0)^{1/2}]/2 \quad (3)$$

in which $[L]_0$ and $[M]_0$ are the total ligand and Mn corrolazine concentrations, respectively. The measured absorbance is then related to [(TBP$_8$Cz)Mn(L)] through eq 4

$$(A - A_0)/(\epsilon_{ML} - \epsilon_M) = [(TBP_8Cz)Mn(L)] \quad (4)$$

in which *A* = absorbance throughout the titration, A_0 = initial absorbance before the addition of L, and ($\epsilon_{ML} - \epsilon_M$) is the difference in the molar absorptivities for the bound and free complex, respectively. We calculated the K_a from a nonlinear least-squares fit of the binding isotherm using eqs 3−4. Because ϵ_{ML} is not known with certainty, the quantity ($\epsilon_{ML} - \epsilon_M$) = $\Delta\epsilon$ was also calculated as part of the fitting procedure.

Scheme 1

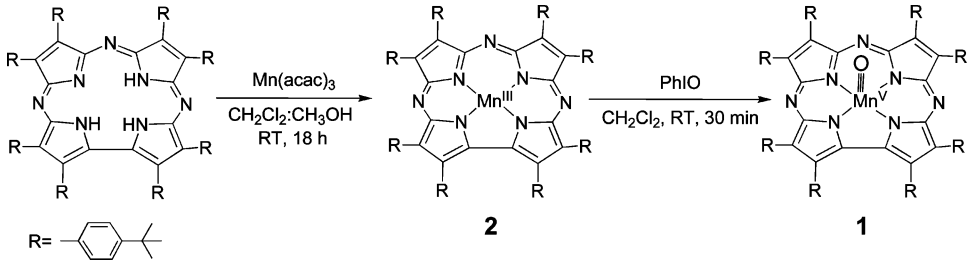

X-ray Absorption Spectroscopy (XAS) Data Collection. Manganese K-edge XAS data were collected at the National Synchrotron Light Source, beam line X9-B (2.8 GeV, ~300 mA). We measured data at 14 K in transmission mode using a Si(111) double crystal monochromator. Samples were diluted in boron nitride (approximately 1:1 volume ratio), ground to homogeneity, and packed into 1-mm-thick Al cells with Kapton windows. We calibrated the energy using $KMnO_4$ as an internal standard, with the $KMnO_4$ pre-edge transition defined as 6543.3 eV, and averaged three or four scans. We normalized the XANES spectra by fitting the data to the McMaster absorption coefficients[30] below and above the edge using a single background polynomial and scale factor.[31] The EXAFS was extracted by first removing a polynomial pre-edge and then subtracting a three region cubic spline with the EXAFS normalized to the Victoreen absorption falloff.

Absorber−scatterer information was obtained from fitting the EXAFS data to eq 5

$$\chi(k) = S_0^2 \sum_s \frac{N_s A_{as}(k)}{kR_{as}^2} \exp(-2k^2\sigma_{as}^2) \sin[2kR_{as} + \phi_{as}(k)] \qquad (5)$$

in which $\chi(k)$ is the fractional modulation in the absorption coefficient above the edge, N_s is the number of scatterers at a distance R_{as}, $A_{as}(k)$ is the effective backscattering amplitude, S_0^2 is a scale factor, σ_{as}^2 is the mean-square deviation in R_{as}, ϕ_{as} is the phase-shift that the photoelectron wave undergoes in passing through the potentials of the absorbing and scattering atoms, and the sum is taken over all shells of the scatterers. The k^3-weighted EXAFS was truncated at 11.7 $Å^{-1}$ because of the presence of a small Fe edge; spectra were analyzed over $k = 3-11.7$ $Å^{-1}$.

The program FEFF 7.02[32] was used to calculate theoretical amplitude and phase functions from the crystallographic data of **2**·(CH_3OH). For the evaluation of the data for **1**, the Mn−O bond length was shortened to 1.55 Å. The scale factor, S_0^2, was held fixed at 0.9. The shift in the threshold energy, ΔE_0, was allowed to vary but was limited to a single ΔE_0 value for all the different shells.

HFEPR Spectroscopy. A sample of **2**·(CH_3OH) was obtained by recrystallization and used for HFEPR studies. The typical amount of **2**·(CH_3OH) was 10 to 15 mg, and the material was trapped in n-eicosane mull to prevent the mechanical torquing of crystallites in the high magnetic field. A recently constructed tunable-frequency HFEPR spectrometer was employed.[33] Tunable frequencies in the 150−700 GHz range (~5−23 cm^{-1} energy) were provided by a set of four backward-wave oscillators. We precalibrated the frequency using a Fabry−Perot resonator. The magnet used was the resistive "Keck" magnet (0−25 T) of improved homogeneity (12 ppm in a 1-cm diameter spherical volume) and temporal stability. We precalibrated the field using an NMR probe and checked the field during the experiment using a DPPH marker. The oversized-pipes wave propagation system was home-built along the principles outlined before.[34] Detection was provided with an InSb hot-electron bolometer. Modulation for detection purposes was provided alternatively either by modulating the magnetic field (1 kHz frequency, 1 mT max amplitude) or by chopping the sub-THz wave beam at ~300 Hz. A Stanford SR830 lock-in amplifier converted the modulated signal to DC voltage.

Electrochemistry and Spectroelectrochemistry. Benzonitrile (PhCN) and pyridine were obtained from Sigma−Aldrich Co., and PhCN was distilled over phosphorus pentoxide (P_2O_5) under vacuum prior to use. CH_2Cl_2 was obtained from EM Science, and was stabilized with an alkene. High purity N_2 was used to deoxygenate the solution before the electrochemical and spectroelectrochemical experiments. Tetra-*n*-butylammonium perchlorate (TBAP) was purchased from Sigma−Aldrich Co., recrystallized from ethyl alcohol, and dried under vacuum at 40 °C for at least one week prior to use. Cyclic voltammetry was conducted with an EG&G model 173 potentiostat. A three-electrode system was used consisting of a glassy carbon working electrode, a platinum counter electrode, and a saturated calomel reference electrode (SCE). Half-wave potentials were calculated from $E_{1/2} = (E_{pa} + E_{pc})/2$ and were referenced to the SCE. For spectroelectrochemical measurements, an optically transparent thin-layer platinum electrode was used as described previously.[35] Time-resolved UV−vis spectra were recorded with a Hewlett−Packard model 8453 diode-array rapid-scanning spectrophotometer.

Results and Discussion

Synthesis. The manganese(III) and manganese(V)−oxo complexes were synthesized according to Scheme 1. The syntheses of both **1** and **2** have been reported in an earlier communication, but in both cases modifications to the procedures have improved the syntheses in terms of convenience and/or yield. In the case of **2**, the metalation procedure initially involved high-temperature conditions in pyridine as solvent. We have since discovered that it is unnecessary to use pyridine, which is toxic and difficult to remove at the end of the reaction, because one can use a CH_2Cl_2/MeOH mixture at room temperature instead; however, the reaction time needs to be increased from 1 h to 18

(30) McMaster, W. H.; Del Grande, N. K.; Mallett, J. H.; Hubbell, J. H. U.S. Department of Commerce Report Number UCRL-50174-SEC 2-R1, U.S. Goverment Printing Office: Washington, DC, 1969.
(31) Weng, T.-C.; Waldo, G. S.; Penner-Hahn, J. E. *J. Synchrotron Radiat.*, in press.
(32) Zabinsky, S. I.; Rehr, J. J.; Ankudinov, A.; Albers, R. C.; Eller, M. J. *Phys. Rev. B* **1995**, *52*, 2995−3009.
(33) Zvyagin, S. A.; Krzystek, J.; van Loosdrecht, P. H. M.; Dhalenne, G.; Revcolevschi, A. *Phys. B (Amsterdam, Neth.)* **2004**, *346−347*, 1−5.
(34) Hassan, A. K.; Pardi, L. A.; Krzystek, J.; Sienkiewicz, A.; Goy, P.; Rohrer, M.; Brunel, L. C. *J. Magn. Reson.* **2000**, *142*, 300−312.
(35) Lin, X. Q.; Kadish, K. M. *Anal. Chem.* **1985**, *57*, 1498−1501.

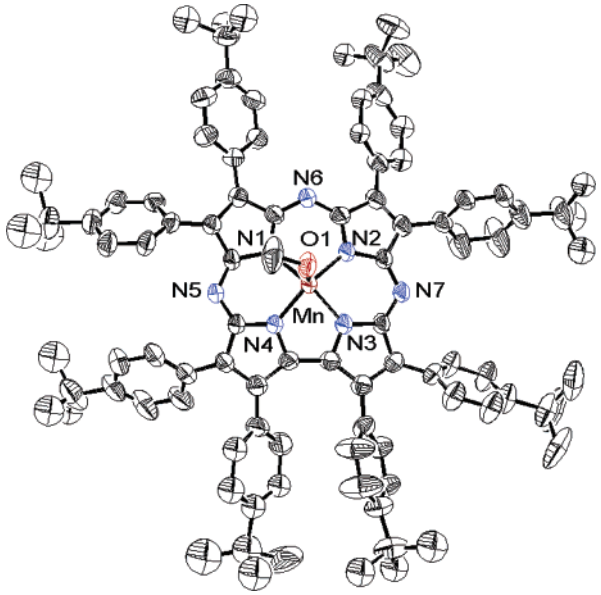

Figure 1. ORTEP diagram of **2**·MeOH. Thermal ellipsoids are drawn at a 30% probability level. Solvent molecules and hydrogen atoms have been omitted for clarity.

h. Chromatographic purification and isolation of **2** were performed in the usual manner. We have also further characterized this compound using elemental analysis, IR data, and a ^{1}H NMR spectrum, which reveals broad, paramagnetically shifted peaks typical of a high-spin manganese(III) complex. After recrystallization from toluene/MeOH, the elemental analysis is consistent with one MeOH present in the crystalline material, as shown in the X-ray structure. However, in routine preparations of **2**, the material obtained after chromatography is typically dried under high vacuum, and UV−vis spectroscopy indicates that this material does not contain coordinated MeOH, as discussed below.

The $Mn^V{\equiv}O$ complex **1** was initially prepared from oxidation of **2** with mCPBA, but care had to be taken to not add excess mCPBA as to avoid the degradation of **2** to unidentified products. The replacement of mCPBA with PhIO gives **2** in comparable yields, and no degradation is seen even with a large excess of PhIO. The limited solubility of PhIO in CH_2Cl_2 also makes it easy to separate from the product. Both of these complexes have now been characterized by X-ray techniques, as described below.

X-ray Crystal Structure of [(TBP$_8$Cz)Mn^{III}(MeOH)]·(C$_7$H$_8$)$_3$. An ORTEP diagram of **2**·(MeOH) is shown in Figure 1, and selected bond distances and angles are given in Table 1. The manganese(III) ion is five-coordinate with a methanol molecule bound in the axial position. In other metallocorrolazines such as [(TBP$_8$Cz)Co(PPh$_3$)],[2] [(TBP$_8$Cz)-Co(py)$_2$] (py = pyridine),[2] and [(TBP$_8$Cz)Co(CCSiPh$_3$)],[5] the macrocycle is relatively planar, with the largest deviation from the least-squares-plane of the 23-atom core being 0.22(1) Å as found in [(TBP$_8$Cz)Co(PPh$_3$)]. For the manganese(III) complex, there is significantly more distortion in the corrolazine core, as shown by the large deviation from the 23-atom plane of ∼0.29 Å for N(3) and N(4) and ∼0.32 Å for C(14) and C(15). This distortion may come from steric

Table 1. Selected Bond Lengths (Å) and Bond Angles (deg) for **2**·MeOH

Mn−N(1)	1.892(4)
Mn−N(2)	1.876(3)
Mn−N(3)	1.885(3)
Mn−N(4)	1.884(3)
Mn−[N(1)−N(4)]$_{plane}$	0.373(2)
Mn−(23-atom)$_{core}$	0.582(1)
C_β−C_β (av)	1.392(1)
C_α−C_β (av)	1.440(1)
C_α−C_α	1.445(6)
Mn−O	2.107(3)
N(1)···N(3)	3.694(5)
N(2)···N(4)	3.683(5)
Mn−O−C(97)	122.8(3)
N(1)−Mn−N(2)	92.76(15)
N(2)−Mn−N(3)	88.58(14)
N(3)−Mn−N(4)	80.59(14)
N(4)−Mn−N(1)	89.10(14)
N(1)−Mn−O	96.92(14)
N(2)−Mn−O	100.92(14)
N(3)−Mn−O	106.45(14)
N(4)−Mn−O	101.83(14)

interactions between the axial methanol molecule and the peripheral TBP groups, which may be enhanced by the hydrogen bonded dimer pairs seen in the packing diagram (Figure 2). The manganese ion is located 0.582(1) Å above the plane of the macrocycle toward the axial MeOH ligand. The metal ion in this case is much further out of the plane than in the analogous five-coordinate cobalt corrolazines, with Co−(plane) = 0.442 Å for [(TBP$_8$Cz)Co(PPh$_3$)] and Co−(plane) = −0.076(1) Å for [(TBP$_8$Cz)Co(CCSiPh$_3$)]. The Mn−N(ave) distance is 1.884(7) Å, which is also longer than the average Co^{III}−N distances of 1.837(8) and 1.838(3) Å for [(TBP$_8$Cz)Co(PPh$_3$)] and [(TBP$_8$Cz)Co(py)$_2$], respectively. The effects of the smaller cavity of a corrolazine as compared to that of a corrole is usually manifested in short M−N$_{pyrrole}$ bond lengths, but for the Mn^{III} complex, the average Mn−N distance is nearly the same as that for the corroles [(E-7,13-MC)Mn^{III} (1.894 Å)[29] and (OEC)Mn^{III}(py) (1.917 Å)].[10] The longer Mn−N$_{pyrrole}$ distances are clearly a consequence of the large out-of-plane displacement of the metal ion.

The Mn−O bond distance to the axial methanol ligand is 2.107(3) Å and is similar to that found for [(OEP)Mn^{III}-

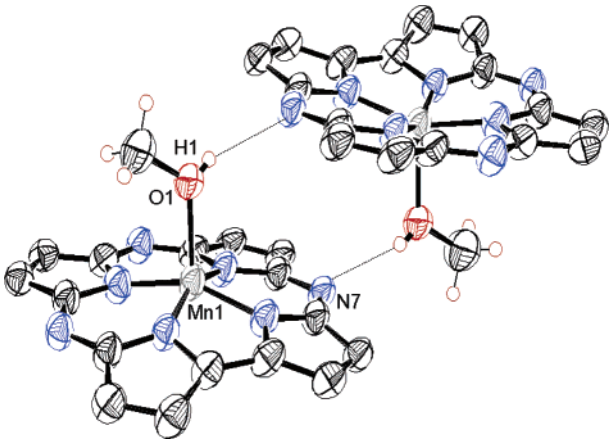

Figure 2. A fragment of the crystal structure of **2**·MeOH showing the hydrogen bonding interaction between two complexes. Solvent and hydrogen atoms (except for the axial MeOH) have been omitted for clarity.

(HOEt)]ClO_4 [Mn−(HOEt) = 2.145 Å].[36] As seen in the packing diagram in Figure 2, the axial MeOH ligands on neighboring corrolazines form hydrogen bonds with adjacent meso nitrogen atoms to give hydrogen bonded dimer pairs. The hydrogen atom of the MeOH ligand was located in the electron density map and refined in position. The distance between the O atom and the meso N atom of 2.764(5) Å and the O−H···N angle of 176.2° are clearly consistent with a hydrogen bond interaction. Corroles[10] and porphyrins[37] often form π-stacked dimer pairs in the crystal lattice, and the first example of a π-stacked corrolazine was recently reported.[5] The hydrogen bonded dimer motif seen for **2**·(CH_3OH) is much less common and demonstrates that the meso nitrogen atoms in the corrolazine are potentially good Lewis basic sites for protonation or possibly even peripheral metalation.

Binding of Axial Ligands to 2. The addition of MeOH to the Mn^{III} complex causes significant changes in the UV−vis spectrum, as seen in Supporting Information Figure S1. These data show that the Mn^{III} starting material is most likely a four-coordinate complex, which converts to the five-coordinate MeOH adduct upon the titration of MeOH in CH_2Cl_2. Although we cannot rule out an alternative interpretation corresponding to the conversion of a five-coordinate (Cz)Mn(MeOH) species to a six-coordinate (Cz)Mn$(MeOH)_2$ species, we believe this mechanism is highly unlikely because of the five-coordinate nature of the X-ray structure for **2**·(CH_3OH) and the similarity of the UV−vis spectra with other donor ligands, such as Ph_3P═O (vide infra).[38] The binding of MeOH is complicated by the possibility of intermolecular hydrogen bonding as indicated by the X-ray structure, and thus a binding constant was not calculated for MeOH. Titration of heterocyclic bases such as pyridine and 1-methylimidazole (1-MeIm) to **2** leads to very small changes (<5 nm shift in the Soret band) in the UV−vis spectrum (data not shown). These small changes appear to increase as the concentration of pyridine or 1-MeIm is increased, suggesting weak coordination to the Mn^{III} ion. However, the changes in the spectrum are too small to give a reliable binding isotherm, and thus quantification of the binding constants was not possible. In contrast, the binding of Cl^-, Et_3PO, or Ph_3PO gives significant changes in the UV−vis spectrum, leading to binding isotherms that can be fit to give binding constants.

The addition of Et_4NCl to **2** in CH_2Cl_2 resulted in changes in the UV−vis spectra as shown in Figure 3, and good isosbestic behavior was observed. The Soret band splits into two peaks at 435 and 480 nm while the Q-band increases in intensity, and a weak shoulder appears at 720 nm. From these

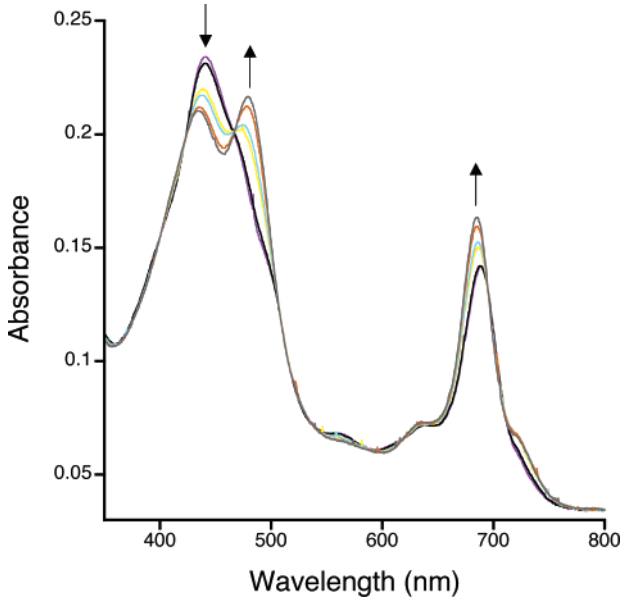

Figure 3. UV−vis titration of tetraethylammonium chloride (0−1.3 equiv) into a solution of **2** (3.33×10^{-6} M) in CH_2Cl_2.

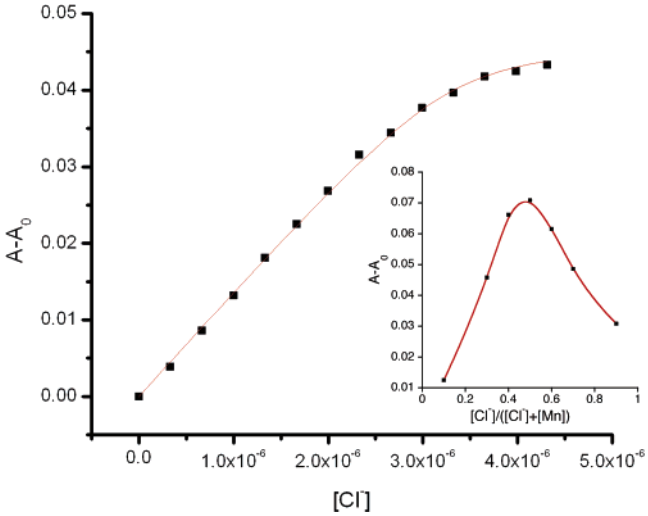

Figure 4. Binding isotherm for the addition of Et_4NCl to **2** in CH_2Cl_2 plotted from the data in Figure 3 at 480 nm. The red line is the best fit of the data to eq 4 in the text, which gives $K_a = 1.34 \times 10^7$ M^{-1} and $\Delta\epsilon = 1.4 \times 10^4$ $M^{-1}cm^{-1}$. Inset: Job's plot showing a maximum at [Cl^-]/([Cl^-] + [Mn]) ≈ 0.5, indicating 1:1 binding stoichiometry.

data, the binding isotherm shown in Figure 4 was obtained, which was fit directly to obtain K_a. We determined the stoichiometry of binding by using Job's method, which yielded a maximum in the Job's plot that indicates a corrolazine to Cl^- ratio of 1:1, as seen in the inset of Figure 4. The equilibrium expression is given in eq 1, along with a definition of the binding constant in eq 2. The K_a was obtained as described in the experimental section. Simpler methods involving a linearization of the equilibrium expression to obtain K_a, such as a Hill plot, are commonly employed for ligand binding to porphyrins and corroles. However, such methods are only useful in cases of relatively weak binding in which $[L_0] - [L] \approx [L_0]$ and as such would not be useful for the strong binding behavior observed for **2**.[39]

(36) Cheng, B. S.; Scheidt, W. R. *Acta Crystallogr., Sect. C* **1996**, *52*, 585−588.

(37) Scheidt, W. R. In *The Porphyrin Handbook*; Kadish, K. M., Smith, K. M., Guilard, R., Eds.; Academic Press: New York, 2000; Vol. 3, pp 49−112.

(38) We have characterized a five-coordinate **2**·DMF (DMF = dimethylformamide) complex by X-ray crystallography. The UV−vis spectrum observed for the addition of DMF to **2** is the same as that seen for the addition of MeOH. All of these data are consistent with a five-coordinate complex for both DMF and MeOH. (Lansky, D. E., Goldberg, D. P. unpublished results).

(39) Webb, S. J.; Sanders, J. K. M. *Inorg. Chem.* **2000**, *39*, 5912−5919.

The best fit to the data for Cl^- gave $K_a = 1.3(4) \times 10^7$ M^{-1}. The binding constant for Cl^- was significantly higher than that for the phosphine oxides Ph_3PO and Et_3PO, which gave binding constants of $7.8(5) \times 10^5$ and $8.6(4) \times 10^5$ M^{-1}, respectively. In comparison, binding constants for four-coordinate manganese corroles have been reported for a series of pyridine ligands and are much smaller (in the range 6−80 M^{-1}), although it was suggested that for these compounds interactions between macrocycles satisfied the preference for five-coordination.[29] For **2**, intermolecular interactions are discouraged by the sterically bulky peripheral phenyl substituents. The high affinity for all three ligands studied is consistent with a "bare" four-coordinate Mn^{III} center.

HFEPR Spectroscopy of 2·(CH_3OH). HFEPR spectroscopy was first used by some of us to obtain EPR spectra from integer-spin (non-Kramers) Mn^{III} ($S = 2$) porphyrin and porphyrazine compounds.[40] This study showed that EPR spectra could be obtained from "EPR-silent" species such as high-spin Mn^{III} compounds, and some detailed properties of the electronic structure of these species were determined. Since that work, multifrequency HFEPR has proven to be a valuable tool for studying other integer-spin, EPR-silent species, including the manganese(III) corroles (tpfc)Mn($OPPh_3$), [tpfc = 5,10,15-tris-(pentafluorophenyl)corrolato][41] and (DEHMC)Mn (DEHMC = 8,12-diethyl-2,3,7,13,17,18-hexamethyl-corrolato).[42] Recently, the multifrequency experiment was extended to a tunable-frequency version, which allows greater precision in determining spin Hamiltonian parameters. By using swept fields (0−25 T) in combination with high (sub-THz) frequencies, we performed a two-dimensional (resonant field vs transition energy) EPR study of the manganese(III)−corrolazine complex, as shown in Figure 5. Each data point corresponds to a single peak in an individual spectrum, and the inset to Figure 5 shows a typical spectrum recorded at 503 GHz (transition energy 16.77 cm^{-1}). At higher resolution, a single-frequency spectrum such as that in the inset to Figure 5 displays a small splitting of the perpendicular turning points in the powder spectrum ($B_0 \parallel x$ or y) which is indicative of a small but nonzero rhombic zero-field splitting parameter E. We simulated the data in Figure 5 according to established procedures[40,43] using the spin Hamiltonian for an $S = 2$ system:

$$H = \beta\, B\cdot\mathbf{g}\cdot S + D[S_z^2 - S(S+1)/3] + E(S_x^2 - S_y^2) \quad (6)$$

The observed resonances were unequivocally attributed to particular transition branches in the $S = 2$ spin manifold. The complex in the solid state is characterized by the following spin Hamiltonian parameters obtained from the simulations using the best fit values: $S = 2$, isotropic $g = 2.00(1)$, $D = -2.60(2)$ cm^{-1}, and $|E| = 0.015(5)$ cm^{-1}.

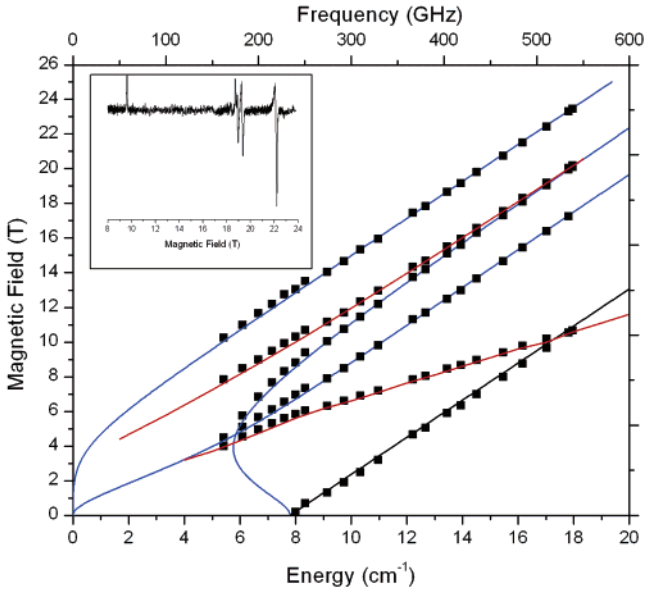

Figure 5. Magnetic field vs transition energy dependence of HFEPR resonances (squares) and simulations using the spin Hamiltonian parameters, as presented in the text. Black lines: parallel turning points; blue lines: perpendicular turning points; and red lines: off-axis turning points in the powder pattern. The small splittings in the perpendicular transitions due to a nonzero E term are not shown for clarity. Inset: single-frequency spectrum at 503 GHz and 10 K. The peak at 19.35 T is due to a $g = 2.00$ impurity that is not reflected in the main plot.

These spin Hamiltonian parameters are within the range of those observed for related Mn^{III} systems, such as Mn(TPP)Cl,[43,44] confirming that **2**·(CH_3OH) is a high-spin $S = 2$, Mn^{III} complex with no evidence for the contribution of a Mn^{II}(corrolazine$^{+\bullet}$) configuration. In particular, the zero-field splitting parameters ($D = -2.60(2)$ cm^{-1}; $|E| = 0.015(5)$ cm^{-1}) are similar to those found for the related Mn^{III} corroles {(tpfc)Mn($OPPh_3$): $D = -2.69(2)$ cm^{-1}, $E = 0.030(3)$ cm^{-1};[41] and (DEHMC)Mn: $D = -2.64(1)$ cm^{-1}, $E = 0.015(5)$ cm^{-1}}.[42] The isotropic g value of ∼2.00 is common for most complexes of manganese(III). In contrast to porphyrins and porphyrazines,[40] corrole and corrolazine complexes of Mn^{III} are not rigorously axial spin systems. More importantly, the magnitude of D is larger for the latter class of complexes. It has been pointed out that the smaller cavity size and higher negative charge of a corrole compared to that of a porphyrin implies a stronger equatorial ligand field, which in turn should lead to a smaller magnitude for D.[42] The larger D values seen for corroles as compared to those of Mn^{III} porphyrins ($1.5 < |D| < 2.5$ cm^{-1}) have been explained as one of the triplet ($S = 1$) excited states ($d_{xy}^1 d_{xz,yz}^3$) lying closer in energy to the quintet ($S = 2$) ground state ($d_{xy}^1 d_{xz,yz}^2 d_{z^2}^1$) in Mn^{III} corrole complexes, which is not the case in porphyrin complexes.[42,43] The ordering of the d orbital energies for these systems is that which was used previously for Mn^{III} corroles[42] and is based on the ordering proposed by Dugad et al. for Mn^{III} porphyrins.[44] The smaller cavity size of the Mn^{III} corrolazine as compared to that of

(40) Goldberg, D. P.; Telser, J.; Krzystek, J.; Montalban, A. G.; Brunel, L. C.; Barrett, A. G. M.; Hoffman, B. M. *J. Am. Chem. Soc.* **1997**, *119*, 8722−8723.
(41) Bendix, J.; Gray, H. B.; Golubkov, G.; Gross, Z. *Chem. Commun.* **2000**, 1957−1958.
(42) Krzystek, J.; Telser, J.; Hoffman, B. M.; Brunel, L. C.; Licoccia, S. *J. Am. Chem. Soc.* **2001**, *123*, 7890−7897.
(43) Krzystek, J.; Telser, J.; Pardi, L. A.; Goldberg, D. P.; Hoffman, B. M.; Brunel, L. C. *Inorg. Chem.* **1999**, *38*, 6121−6129.
(44) Dugad, L. B.; Behere, D. V.; Marathe, V. R.; Mitra, S. *Chem. Phys. Lett.* **1984**, *104*, 353−356.

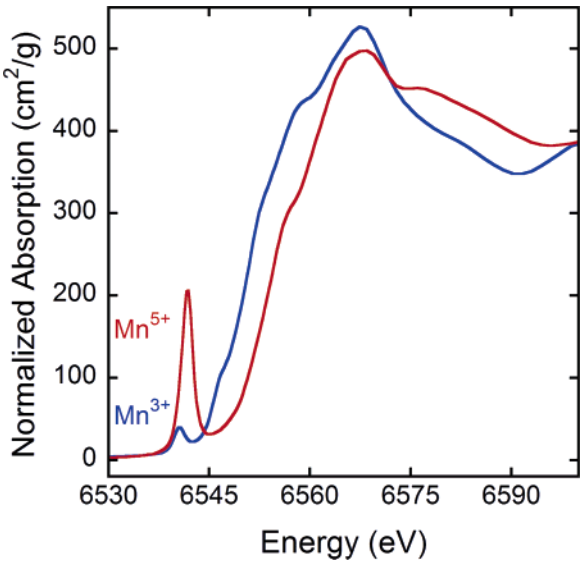

Figure 6. Normalized Mn XANES spectra for **2** (blue line) and **1** (red line). Both spectra are plotted on the same scale.

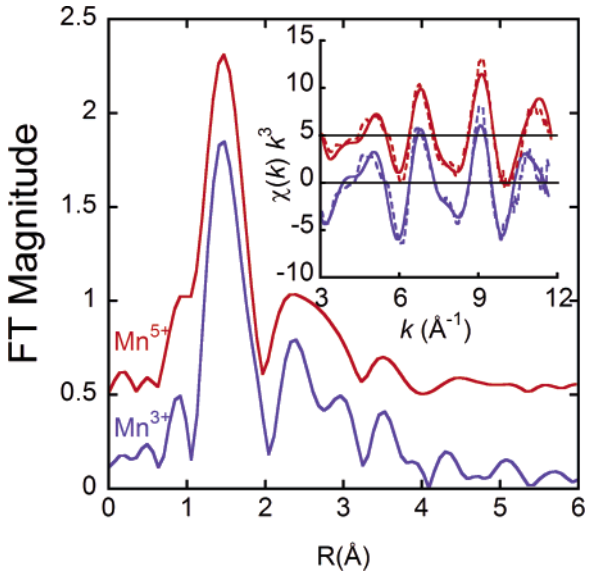

Figure 7. Fourier transform of **2** (blue line) and **1** (red line). Inset: EXAFS data (solid line) and fit (dashed line) for **2** and **1**. Spectra are offset vertically for clarity.

corroles is alleviated at the manganese center by increasing the distance of the manganese ion to the plane formed by the pyrrole N atoms; the Mn displacement in **2**·(CH_3OH) is 0.373(2) Å, compared to 0.29 Å in (tpfc)Mn($OPPh_3$), and the average Mn−N distances in these two complexes are approximately the same. Thus, the equatorial and axial (MeOH vs Ph_3PO) ligand fields are similar in these two complexes, yet the magnitude of D is slightly smaller for **2**·(CH_3OH). This difference may come from a larger energy separation of the triplet-quintet states in the corrolazine complex. The HFEPR data confirm the spin and oxidation state of the Mn ion in **2**·(CH_3OH) as Mn^{III} ($S = 2$) and demonstrate that the corrolazine ligand field is different from that of porphyrins, being much closer to that of corroles.

XANES/EXAFS Results. The XANES spectra of **1** and **2**·(CH_3OH) are shown in Figure 6. The sample of the Mn^{III} complex was crystallized from CH_3OH/toluene as described in the experimental section and thus contained the axial MeOH ligand seen in the crystal structure. There is a shift of ~4 eV going from Mn^{III} to Mn^{V}, which is consistent with the oxidation of Mn.[45] One of the most striking features of the XANES spectra is the intense pre-edge transition that is observed for **1**. Such an intense pre-edge feature has been seen for oxo− and nitrido−porphyrin complexes, as well as for the crystallographically characterized complex Na[Mn^{V}≡O(HMPAB)] [HMPAB = 1,2-bis(2-hydroxy-2-methyl-propan-amido)benzene], which was synthesized by Collins and co-workers.[45] This feature can be attributed to a 1s → ($M_{3d} + O_{2p-\pi}$) transition.[46]

The most prominent feature of the Fourier transforms of both samples is the peaks at $R + \alpha \approx 1.5$ Å (Figure 7).

Table 2. Curve Fitting Results for XANES/EXAFS Data[a]

sample	coord no.	R_{ab} (Å)[b]	σ^{2c}	coord no.	R_{ab} (Å)[b]	σ^{2c}	coord no.	R_{ab} (Å)[b]	σ^{2c}	ΔE_0	F[d]
Mn(III)	4N	1.89	1.5				8C	2.89	3.5	3.0	211
	4N	**1.90**	**1.6**	**1O**	**2.19**	**6.4**	**8C**	**2.89**	**3.6**	**3.1**	**190**
	4N	1.89	1.5	1O	1.47	4.5	8C	2.90	3.5	4.0	205
Mn(V)	4N	1.86	1.3				6C	2.84	3.7	−3.5	387
	4N	**1.88**	**2.8**	**1O**	**1.56**	**1.8**	**6C**	**2.90**	**4.1**	**7.3**	**117**
	4N	1.85	1.5	1O	2.20	4.8	6C	2.83	4.1	−6.9	348

[a] Fits to unfiltered data. Best fits are shown in bold. [b] Absorber−scatterer distance. [c] Debye−Waller factor (Å^2) × 10^3. [d] $F = \sum(\chi_{exp} - \chi_{calc})^2 k^6$. The accuracy in the determination of the bond lengths is approximately 0.02 Å, and the precision is 0.004 Å.

These are due to scattering from four first shell nitrogens. Although both Fourier transforms show only a single first shell peak, it was not possible to fit the data for either complex without including an additional nearest neighbor scatterer together with at least one shell of outer shell scatterers representing the Mn−$C_{corrolazine}$ interaction. The best three shell fits are shown in Figure 7, and the fit results are summarized in Table 2. The refined Mn−N distances were virtually identical for the two samples, reflecting the rigidity of the corrolazine ring. In the case of the Mn^{III} complex, the first shell peak is asymmetric at higher R, suggesting the presence of a long Mn−O distance as is seen in the crystal structure. Consistent with this, the data could be modeled with a Mn−O distance of 2.19 Å. The agreement with the Mn−O distance found crystallographically (2.107 Å) is relatively poor, perhaps reflecting the difficulty of refining the position of one weak scatterer in the presence of four stronger scatterers. Attempts to include a short Mn−O interaction in place of the 2.2-Å Mn−O distance gave worse fits and unrealistically large Debye−Waller factors.

To properly fit the (Cz)Mn^{V}≡O data, it was necessary to include a short Mn−O distance that refined to 1.56 Å. Inclusion of a long Mn−O distance in place of the short Mn−O gave fits that were three times worse and resulted in an unrealistic shift in ΔE_0. The 1.56-Å distance obtained from

(45) Weng, T.-C.; Hsieh, W.-Y.; Uffelman, E. S.; Gordon-Wylie, S. W.; Collins, T. J.; Pecoraro, V. L.; Penner-Hahn, J. E. *J. Am. Chem. Soc.* **2004**, *126*, 8070−8071.
(46) Penner-Hahn, J. E.; Benfatto, M.; Hedman, B.; Takahashi, T.; Doniach, S.; Groves, J. T.; Hodgson, K. O. *Inorg. Chem.* **1986**, *25*, 2255−2259.

the best fit for **1** is in excellent agreement with the Mn−O distance determined by X-ray crystallography for Na[Mn^{V}≡O(HMPAB)] (Mn−O = 1.548 Å)[47] and the related complexes [Mn^{V}≡O(PHAB)]$^{-}$ [PHAB = 1,2-bis(2,2-diphenyl-2-hydroxyethanamido)benzene; Mn−O = 1.558(4) Å][48] and [Mn^{V}≡O(tetraamido)]$^{-}$ [Mn−O = 1.549(3) Å][49] and is thus consistent with the presence of a triply bonded Mn^{V}≡O unit. The features at higher *R* for both data sets are due to single and multiple scattering involving the corrolazine. Six and eight carbons were also included in the models, but no attempt was made to model the multiple scattering.

Although inclusion of a short Mn−O distance is necessary to fit the EXAFS data for **1**, there is no well-defined peak for the Mn^{V}≡O unit in the low-*R* region in Figure 7. Similar results were obtained for Na[Mn^{V}≡O(HMPAB)], which was fit with a short metal−oxo bond but did not exhibit a Mn^{V}≡O peak in the Fourier transform, and it was concluded that it is difficult to determine the presence of a short Mn−O bond on the basis of EXAFS fitting alone.[45] However, as mentioned above, M≡E species with d^0-d^2 configurations (e.g., M = Ti, V, Cr; E = O, N) and short M≡E distances exhibit the common feature of an intense pre-edge peak in the XANES spectrum, which provides a definitive signature for the presence of a Mn^{V}≡O moiety.[45] In contrast, XANES spectra for a Mn^{IV}−oxo (d^3) porphyrin showed a significantly attenuated pre-edge peak.[50] The combined results from the EXAFS fitting and the XANES data provide unambiguous identification of the Mn^{V}≡O unit in **1**, with a metal−oxo bond distance of 1.56(2) Å. The area under the pre-edge peak is identical to that found previously for Na[Mn^{V}≡O(HMPAB)], indicating that the Mn^{V}≡O species accounts for essentially all of the manganese present in the bulk material.

Electroreduction of 2. The electrochemistry of **2** was examined in both PhCN and pyridine. Representative cyclic voltammograms are shown in Figure 8, and the half-wave or peak potentials (referenced to SCE) are summarized in Table 3. A proposed mechanism for the different electrochemical transformations of **2** is shown in Scheme 2 and is based in part on the spectroelectrochemistry data in which E_{app} = the applied potential in the thin-layer cell (vide infra). Two reversible oxidations and one reversible reduction are seen in PhCN, whereas in pyridine there are two reversible reductions and one irreversible oxidation. There are also several additional irreversible reduction processes in PhCN as seen in Figure 8a. The first reversible reduction of **2** occurs at $E_{1/2}$ = −0.91 V in both PhCN and pyridine. A second reduction is also seen at similar potentials of E_{pc} = −1.50 V in PhCN and $E_{1/2}$ = −1.50 V in pyridine. The peak currents for the first two reductions (at −0.91 and −1.50 V) are approximately equal in PhCN, but in pyridine the first reduction peak current is approximately double that of the second, which may suggest two electrons are added in the first step under these solution conditions.

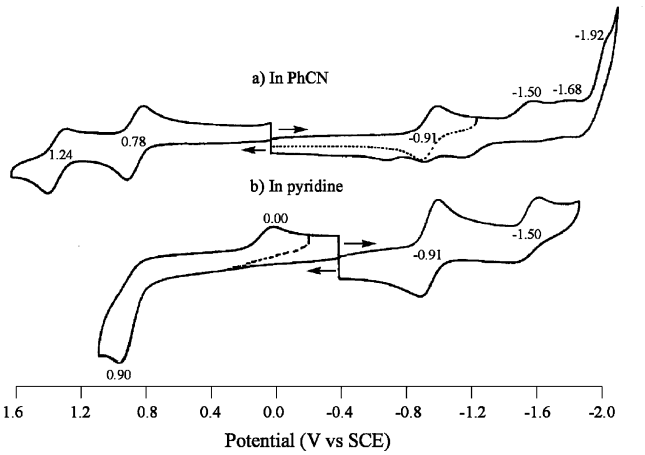

Figure 8. Cyclic voltammograms of **2** in PhCN and pyridine containing 0.1 M TBAP. Scan rate = 0.10 V/s.

Table 3. Half-Wave Potentials (V vs SCE) in Different Solvents Containing 0.1 M TBAP

		oxidation		reduction			
compound	solvent	2nd	1st	1st	2nd	3rd	4th
$(TBP_8Cz)Mn^{III}$ (**2**)	PhCN	1.24	0.78	−0.91	−1.50[a]	−1.68[a]	−1.92[a]
	pyridine		0.90[b]	−0.91	−1.50		
$(TBP_8Cz)Mn^{V}$≡O (**1**)	PhCN	1.52[b]	1.09	0.02	−1.17	−1.66[a]	−1.89[a]
	pyridine			0.03	−0.91	−1.15	−1.70[a]
	CH_2Cl_2	1.57[b]	1.02	−0.05	−1.20	−1.71	

[a] E_{pc} at scan rate = 0.1 V/s. [b] E_{pa} at scan rate = 0.1 V/s.

Time-resolved thin-layer UV−vis spectra were obtained during the first reduction of **2** at a controlled-potential of −1.30 V vs SCE. Two sets of spectral changes with different isosbestic points are seen in PhCN (Figure 9a), suggesting two different sets of equilibria and a possible ECE type electrochemical mechanism [an electron transfer (E) followed by a chemical step (C) and then another electron transfer (E)]. The first set of spectral changes occurs from 0 to 150 s of controlled-potential electrolysis, and the second occurs from 150 to 340 s. In the initial process, the Soret band at 448 nm decreases and splits into two bands at 433 and 474 nm. The Q-band at 693 nm also decreases slightly in intensity and blue-shifts to 685 nm. In the second step (t = 150−340 s), the Soret band becomes broader and decreases in intensity as a shoulder grows in at 532 nm. More significant changes are seen in the visible region of the spectrum where the band at 685 nm disappears and is replaced by a broad band centered at 766 nm. The final spectrum of the reduction process in PhCN after 340 s is similar to the final UV−vis spectrum obtained in pyridine via the single one-step reduction process at an applied potential of −1.20 V. This is shown in Figure 9b. Further reduction of **2** at an applied potential of −1.60 V in either solvent (PhCN or pyridine) gives identical spectral changes, with a loss of the broad peaks in both the UV (∼460 nm) and the visible (∼766 nm)

(47) Collins, T. J.; Gordon-Wylie, S. W. *J. Am. Chem. Soc.* **1989**, *111*, 4511−4513.
(48) MacDonnell, F. M.; Fackler, N. L. P.; Stern, C.; O'Halloran, T. V. *J. Am. Chem. Soc.* **1994**, *116*, 7431−7432.
(49) Miller, C. G.; Gordon-Wylie, S. W.; Horwitz, C. P.; Strazisar, S. A.; Peraino, D. K.; Clark, G. R.; Weintraub, S. T.; Collins, T. J. *J. Am. Chem. Soc.* **1998**, *120*, 11540−11541.
(50) In this work, an intense pre-edge transition was observed for a Mn^{V}(N) porphyrin and compared to the weak pre-edge feature of a Mn^{IV}═O porphyrin. Ayougou, K.; Bill, E.; Charnock, J. M.; Garner, C. D.; Mandon, D.; Trautwein, A. X.; Weiss, R.; Winkler, H. *Angew Chem., Int. Ed. Engl.* **1995**, *34*, 343−346.

Scheme 2

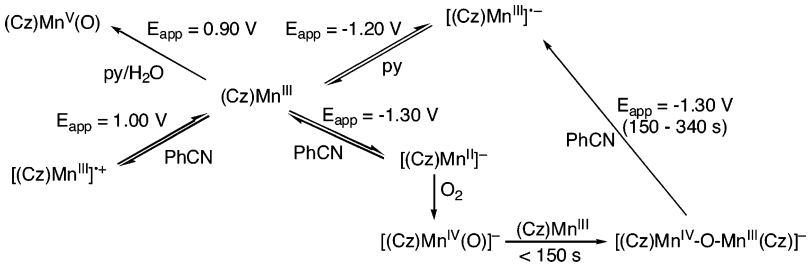

regions and a slight increase near 420 nm (Supporting Information Figure S2).

The spectroelectrochemical results indicate that the final product of the first reduction of **2** (−0.91 V) is the same species in both PhCN and pyridine. This product is characterized by a broad band at 766 nm that points to a compound with π-anion-radical character, $[(Cz)Mn^{III}]^{\bullet-}$.[51,52] In PhCN, an intermediate species appears from 0 to 150 s (Figure 9a), which has a spectrum similar to that seen for the product formed by the chemical reduction of **1** with cobaltocene in a toluene/CH_2Cl_2 mixture, and is tentatively assigned as a mixed-valence dimeric species, $[(Cz)Mn^{IV}(\mu\text{-}O)Mn^{III}(Cz)]^-$, on the basis of EPR spectroscopy (vide infra). A mixed-valence dimer that is more oxidized than the starting material could form if the initial reduction of **2** in PhCN produces a transient, highly unstable $[(Cz)Mn^{II}]^-$ species that is then immediately reoxidized to $[(Cz)Mn^{IV}(O)]^-$ by adventitious oxygen, which in turn combines with $(Cz)Mn^{III}$ to give a

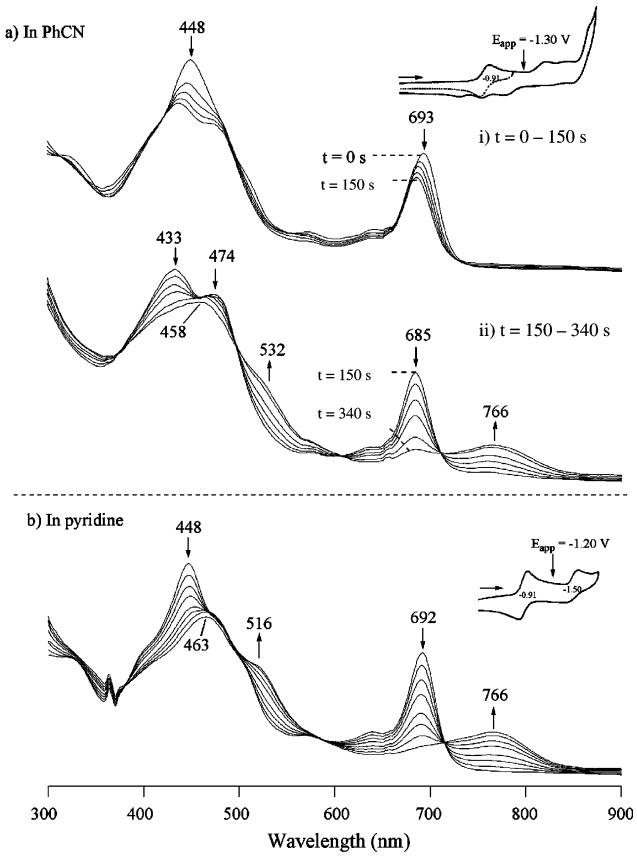

Figure 9. Time-resolved thin-layer UV−vis spectra during (a) the first reduction of **2** at −1.30 V in PhCN from 0 to 150 s (i), and from 150 to 340 s (ii) and (b) the first reduction in pyridine at −1.20 V.

μ-oxo dimer in solution (Scheme 2). Related dimer formations have been shown in the case of (TPP)Mn (TPP = tetraphenylporphyrin).[53−55] Although the mechanism of dimer formation in Scheme 2 is speculative, and indeed the intermediate in the first step in Figure 9a may be an unidentified species, it is reasonable to assume that this first step is associated with a metal-centered redox process given the small changes in the UV−vis spectrum, which contrast with the large changes that are associated with a ligand-centered process (π-anion radical formation at 340 s in Figure 9a).

Electrooxidation of 2. The first and second oxidations of **2** in PhCN appear at $E_{1/2} = 0.78$ and 1.24 V, respectively, and are reversible one-electron-transfer processes. This contrasts with what is seen in pyridine in which the first oxidation is an irreversible multielectron process at $E_{pa} = 0.90$ V (Figure 8b). Quite different UV spectral changes are also observed during the first controlled-potential oxidation of the Mn^{III} complex in the two solvents, and these spectral changes are illustrated in Figure 10a.

The reversible one-electron oxidation of **2** at $E_{app} = 1.00$ V in PhCN leads to a UV−vis spectrum having a broad band at 784 nm, which suggests formation of a corrolazine π-cation radical. In contrast, controlled-potential oxidation of the same compound in pyridine at 0.90 V involves more than one electron and leads to a species with blue-shifted Soret and Q-bands located at 420 and 633 nm, respectively. No π-cation-radical-type bands are observed between 700 and 900 nm, and the final spectrum closely resembles the spectrum of unreacted **1** in the same solvent (Figure 10b). These data clearly suggest that the irreversible electrooxidation of **2** in pyridine leads to the electrochemically initiated conversion of **2** to **1**.

Further evidence for a Mn^{III} to Mn^{V}−oxo conversion is provided by the cyclic voltammogram of **2** in pyridine (Figure 8 and inset of Figure 10a). Here an irreversible cathodic wave at $E_{pc} = 0.00$ V is seen after one scans through the first irreversible oxidation. The peak potential of this new reduction process matches closely the peak potential for the

(51) Mack, J.; Stillman, M. J. *J. Am. Chem. Soc.* **1994**, *116*, 1292−1304.
(52) Kadish, K. M.; Liu, H. Y.; Anderson, J. E. *Inorg. Chim. Acta* **1989**, *163*, 201−205. Similar spectral changes are observed during the one-electron reduction of a phosphorus(V) corrolazine, and the formation of a π-anion radical product was verified by ESR spectroscopy (unpublished results).
(53) Razenberg, J. A. S. J.; Van der Made, A. W.; Smeets, J. W. H.; Nolte, R. J. M. *J. Mol. Catal.* **1985**, *31*, 271−287.
(54) Camenzind, M. J.; Schardt, B. C.; Hill, C. L. *Inorg. Chem.* **1984**, *23*, 1984−1986.
(55) Schardt, B. C.; Hollander, F. J.; Hill, C. L. *J. Am. Chem. Soc.* **1982**, *104*, 3964−3972.

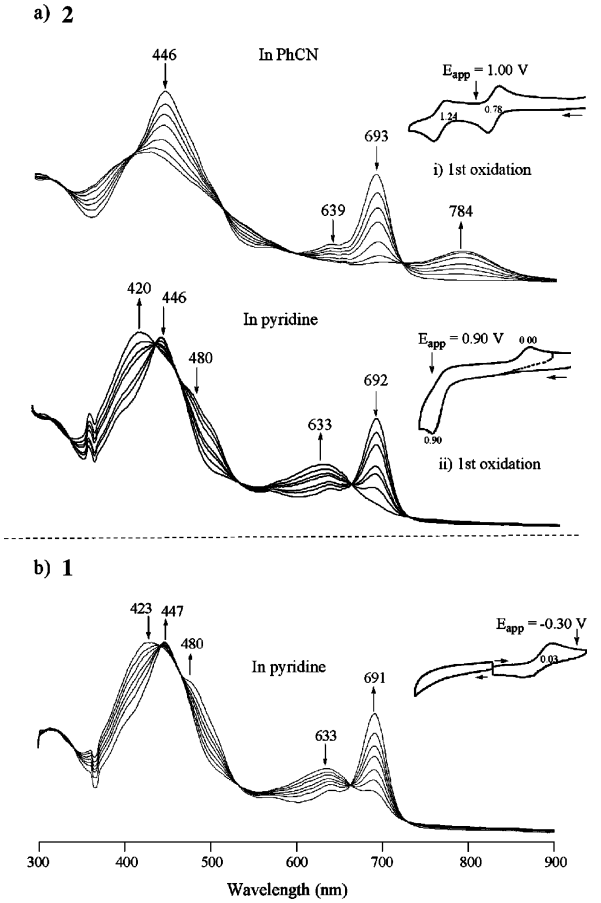

Figure 10. Time-resolved thin-layer spectral changes of (a) **2** during the first oxidation in PhCN at 1.00 V and pyridine at 0.90 V and (b) **1** during reduction in pyridine at −0.30 V, 0.1 M TBAP.

first reduction of **1** in either solvent (vide infra). Taken together, the electrochemical and spectroelectrochemical data are self-consistent and point to the formation of **1** in pyridine upon the oxidation of the Mn^{III} corrolazine. The fact that this conversion takes place in pyridine and not in PhCN is also consistent with the properties of the two solvents. Trace water, which is the most likely source of the terminal oxo group in **1**, can be expected to be in higher concentration in pyridine than in PhCN. In addition, pyridine, as opposed to PhCN, can serve as a base to help deprotonate the coordinated water and form the oxo complex.

Electroreduction of 1. The electrochemistry of **1** was examined in PhCN, pyridine, and CH_2Cl_2. Cyclic voltammograms of these three solvents are illustrated in Figure 11, and the half-wave or peak potentials are summarized in Table 3. A proposed mechanism for the different electrochemical transformations of **1** is shown in Scheme 3 in which E_{app} represents the applied potential in the thin-layer spectroelectrochemistry experiments described below. In all three solvents the compound exhibits a reversible to quasireversible reduction at potentials close to 0.0 V vs SCE, and the position of this reduction strongly suggests a metal-centered process, that is, $Mn^{V} \rightarrow Mn^{IV}$.

Time-resolved thin-layer spectra obtained during the reduction of the Mn^{V}−oxo complex in pyridine and PhCN are shown in Figures 10b and 12, respectively. The data in

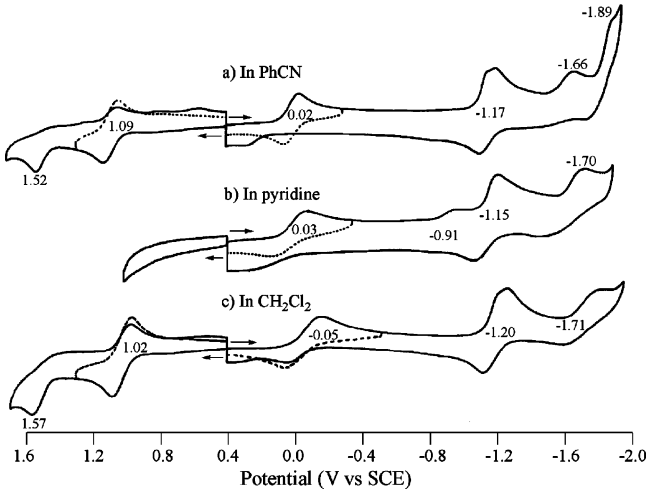

Figure 11. Cyclic voltammograms of **1** in PhCN (a), pyridine (b), and CH_2Cl_2 (c), 0.1 M TBAP at a scan rate of 0.1 V/s.

Figure 10b for the first reduction of **1** in pyridine (E_{app} = −0.30 V) show quite clearly that **2** is the final product. This species has bands at 447, 480, and 691 nm, and these bands are identical to those observed in Figure 10a for the Mn^{III} compound in pyridine. Formation of the Mn^{III} complex is also supported by thin-layer cyclic voltammetry in pyridine, in which the bulk material is undergoing redox conversions (Supporting Information Figure S3). On the first scan, four reductions at −0.02, −0.93, −1.18, and −1.52 V are observed. However, on the second scan, the two reductions at −0.02 and −1.18 V disappear, and only the two located at $E_{1/2}$ = −0.93 and −1.52 V remain. Both $E_{1/2}$ values are close to the half-wave potentials for the reduction of **2** in the same solvent, that is, −0.90 and −1.50 V vs SCE (see Figure 8).

Different results are seen during the reduction of **1** in PhCN. As illustrated in Figure 12a, the Soret band at 425 nm decreases and red-shifts to 436 nm as a new band at 475 nm grows in; at the same time the visible band at 633 nm disappears and a new, more intense visible band at 685 nm is formed. The final UV−vis spectrum has bands at 434, 472, and 685 nm and looks quite similar to the spectrum of the in-situ-generated $[(Cz)Mn^{IV}(\mu\text{-}O)Mn^{III}(Cz)]^{-}$ obtained after the chemical reduction of **1** with cobaltocene (see Figure 13a). However, attempts to generate the same μ-oxo dimer by the bulk electrolysis of **1** were unsuccessful.

The second controlled-potential reduction of **1** at −1.30 V shows two sets of spectral changes, each of which is accompanied by well-defined isosbestic points (Figure 12b). The first occurs from 0 to 60 s, and the second occurs from 60 to 160 s. The initial set of spectral changes is characterized by a decrease in the split Soret band at 436 nm, an increase in the band at 473 nm, and a slight increase in the intensity of the visible band at 683 nm. The shape and position of the bands in this spectrum closely resemble those in the spectrum obtained during either the first reduction of **1** (Figure 12a) or the first reduction of **2** (Figure 9). In contrast, the spectral changes between 60 and 160 s are more pronounced (Figure 12b), and the final spectrum has bands at 478, 518, and 792 nm.

Scheme 3

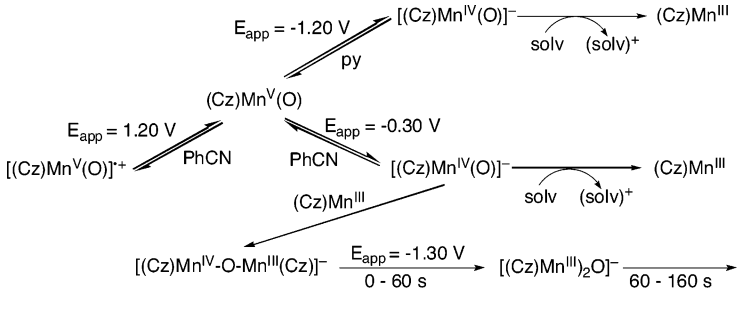

All of the above data are consistent with a mechanism in which the first reduction product of **1** is a transient, highly unstable Mn^{IV}−oxo complex. It is reasonable to expect that the Mn^{IV}−oxo species would be highly reactive because it is a high-spin d^3 metal−oxo, as compared to the low-spin d^2 configuration of the metal−oxo unit of **1**. In the case of pyridine, this species then abstracts an electron from the solvent to give a Mn^{III} complex, resulting in a smooth transition from $(Cz)Mn^{V}{\equiv}O$ to $(Cz)Mn^{III}$. However, in the case of PhCN, evidence of the formation of the dimeric $[(Cz)Mn^{IV}(\mu\text{-}O)Mn^{III}(Cz)]^-$ is observed at $E_{app} = -0.30$ V (Figure 12a). As shown in Scheme 3, this mixed-valence dimer may form via the reduction of $(Cz)Mn^{V}{\equiv}O$ to $[(Cz)Mn^{IV}(O)]^-$, which can either abstract an electron from the solvent to give $(Cz)Mn^{III}$ as it does in pyridine or react with the $(Cz)Mn^{III}$ as it is formed in PhCN to give the mixed-valence dimer. At a more negative applied potential ($E_{app} =$ −1.30 V), the reduction of $[(Cz)Mn^{IV}(\mu\text{-}O)Mn^{III}(Cz)]^-$ to $[(Cz)Mn^{III}(\mu\text{-}O)Mn^{III}(Cz)]^{2-}$ is possibly the first step (0 to 60 s) in Figure 12b, followed by further reduction to a π-anion-radical species (60 to 160 s) that is either monomeric or dimeric in nature.

It is interesting to note that the electrochemically generated μ-oxo dimer only forms during the electroreduction of **1** or **2** in PhCN and not in pyridine. This result is consistent with

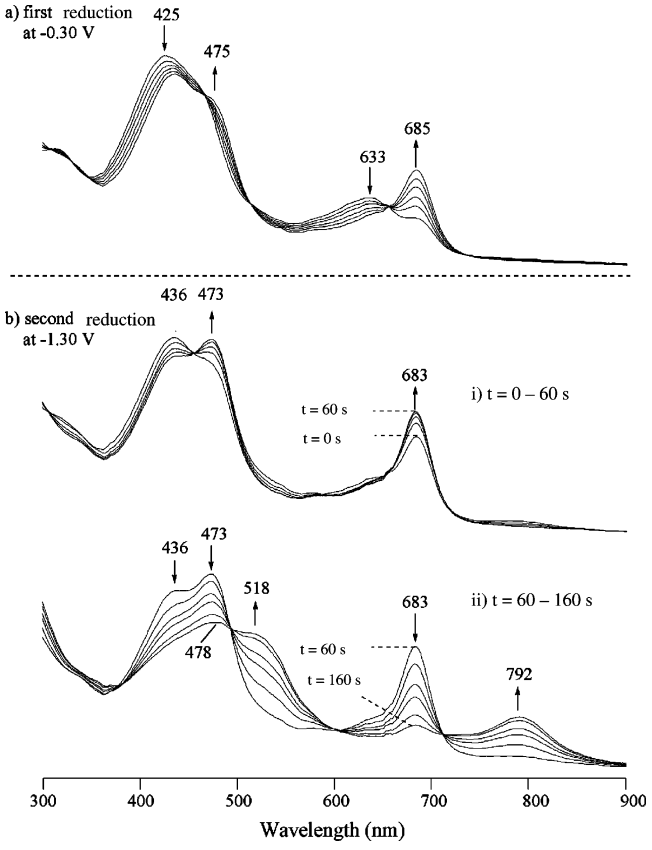

Figure 12. Time-resolved, thin-layer UV−vis spectra of **1** during reductions in PhCN. (a) First reduction at −0.30 V and (b) second reduction at −1.30 V.

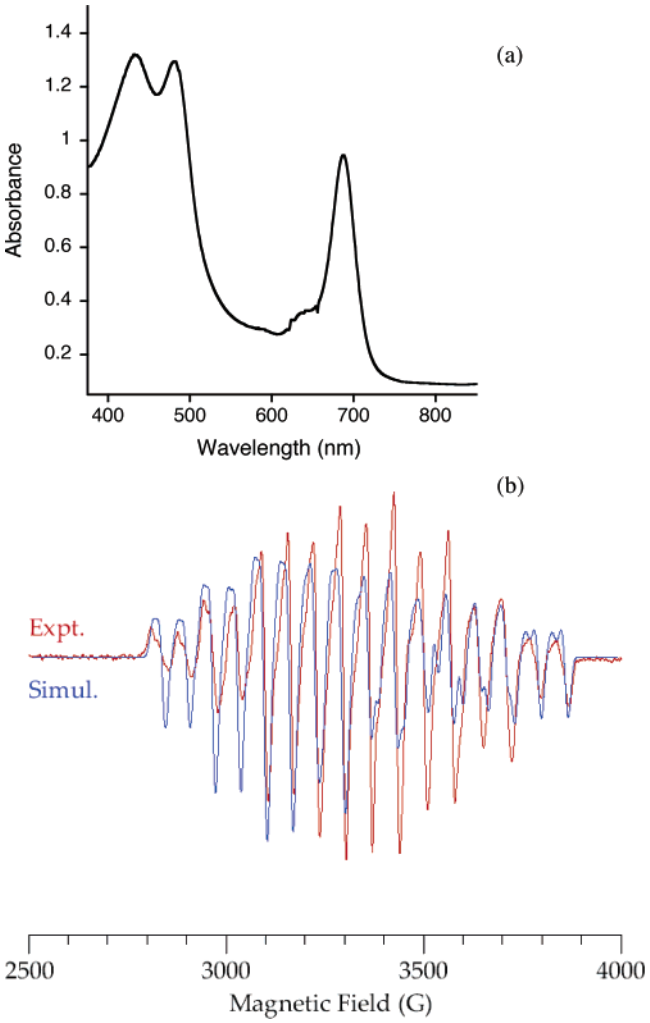

Figure 13. Spectral data for the reaction mixture **1** + excess Cp_2Co in toluene/CH_2Cl_2 (90:10; v:v). (a) UV−vis spectrum and (b) X-band EPR spectrum at 23 K (red line) and simulation (blue line). Instrument settings: microwave frequency = 9.476 GHz; microwave power = 2.0 mW; 100 kHz modulation amplitude = 0.10 G. Simulation parameters: $S = 1/2$, $g_\perp = 2.015$, $g_\parallel = 2.035$, $A(^{55}Mn^{III}) = 390$ MHz, and $A(^{55}Mn^{IV}) = 185$ MHz; single-crystal Gaussian line widths: 25 MHz.

the fact that PhCN is a poor axial ligand compared to pyridine. The latter solvent most likely binds to one or both axial ligand positions of the intermediates formed during the electroreduction of **1** or **2**, preventing dimer formation.

Electrooxidation of 1. Complex **1** exhibits two oxidations in both PhCN and CH_2Cl_2 (Figure 11). The first is reversible, and the second is irreversible. The reversible oxidation potentials are located at $E_{1/2} = 1.09$ V in PhCN and 1.02 V in CH_2Cl_2, whereas the irreversible peak potentials are located at $E_{pa} = 1.52$ and 1.57 V in either PhCN or CH_2Cl_2. No oxidations can be seen in pyridine because of the limited anodic potential window in this solvent. The time-resolved UV spectral changes obtained during the first oxidation of **1** at 1.20 V in PhCN are illustrated in Supporting Information Figure S4. There is a decrease in the intensity of the Soret and visible bands, and a new, weak band appears at 718 nm. These spectral changes are consistent with a ring-centered oxidation.

Chemical Reduction of 1 to Generate [(Cz)Mn^{IV}(μ-O)-Mn^{III}(Cz)]$^-$. The chemical reduction of **1** was attempted with the goal of generating and trapping a Mn^{IV} species. Manganese(IV) ($S = 3/2$) porphyrins have been characterized previously by EPR spectroscopy.[56,57] The addition of one equivalent of Cp_2Co ($E_{1/2} = -1.33$ V)[58] to **1** in a solution of toluene/CH_2Cl_2 (90:10) led to an immediate color change from green to brown, and the UV−vis spectrum of this solution is shown in Figure 13a. This solution was allowed to mix for 1−2 min before being transferred to an EPR tube and rapidly frozen in liquid nitrogen. The X-band EPR spectrum of this solution at 23 K is shown in Figure 13b. To our surprise, the pseudo-16-line pattern shown in Figure 13b was obtained. This pattern is not consistent with a monomeric Mn^{IV} porphyrin but is quite similar to the spectrum obtained for mixed-valent $Mn^{III}Mn^{IV}$(μ-oxo) dimers that contain an $S = 3/2$ Mn^{IV} ion antiferromagnetically coupled with an $S = 2$ Mn^{III} ion to give $S_{total} = 1/2$ as the ground state.[54] On the basis of this precedent, the UV−vis spectrum in Figure 13a is assigned to [(Cz)Mn^{IV}(μ-O)Mn^{III}(Cz)]$^-$, which is the same species proposed to form during the electroreduction of **1** and **2** (vide supra).

A satisfactory simulation of the EPR spectrum (blue line in Figure 13b) was calculated for a $S = 1/2$ system with hyperfine coupling to the two different ^{55}Mn nuclei treated via exact diagonalization of the spin Hamiltonian matrix. Slight axial anisotropy in the g value was included ($g_\perp = 2.015$, $g_\parallel = 2.035$). A good simulation was obtained without including anisotropy in the hyperfine coupling to either $^{55}Mn^{III}$ or $^{55}Mn^{IV}$ [$A(^{55}Mn^{III}) = 390$ MHz; $A(^{55}Mn^{IV}) = 185$ MHz], although in reality there is likely some anisotropy for $^{55}Mn^{III}$.[59] The ratio of the hyperfine coupling of the two ^{55}Mn nuclei is 2.1:1, which is exactly what was found for other $Mn^{III}Mn^{IV}$ oxo-bridged dimers.[54] The isotropic $A(^{55}Mn)$ values are nearly identical with those reported by Hureau et al. for similar species.[59] The hyperfine coupling constants found here for both Mn^{III} and Mn^{IV} are roughly 10−20% smaller than those found for $Mn^{III}Mn^{IV}$ bis(μ-oxo) dimers that lack ligands with extensive (macrocyclic) π-conjugation [e.g., 2,2′-bipyridine (∼470, 220 MHz)[60] or *N*,*N*′-dimethyl-*N*,*N*′-bis(2-pyridylmethyl)ethane-1,2-diamine (436 MHz, 234 MHz)[61]]. The reduction in manganese hyperfine coupling can be qualitatively assigned to a greater covalency in ligand−metal bonding for the corrolazine ligand and hence larger spin delocalization.

The UV−vis spectrum in Figure 13a exhibits a split Soret band at 435 and 482 nm and a Q-band at 685 nm. This spectrum is similar to what is seen upon the electrochemical reduction of **1** in PhCN (Figure 12). Thus, the initial product of the one-electron reduction by Cp_2Co is likely a Mn^{IV}−oxo species, which is highly unstable and undergoes further reactions, ultimately producing the $Mn^{III}Mn^{IV}$ (μ-oxo) dimer observed by X-band EPR. It is also possible that there are other products from this reaction that are EPR-silent at X-band.

Conclusions

The improved synthesis of manganese(III) and manganese(V)−oxo corrolazine complexes has been accomplished. Characterization of the manganese(III) complex **2** by X-ray crystallography revealed the preference of the Mn^{III} ion in a corrolazine for five-coordination. This structure is different from that of a Mn^{III} corrole, in which four-coordination was found.[29] The preference for five-coordination in Mn^{III} corrolazines is also clearly revealed by the strong binding of axial ligands (Cl^-, Et_3PO, and Ph_3PO) to **2** in solution. The electronic structure of **2** has been investigated by HFEPR, which has demonstrated that the complex has an $S = 2$ ground state, but a relatively low lying $S = 1$ excited state, indicative of the strong ligand field of corrolazines.

The manganese(V)−oxo complex, **1**, has not yet been characterized by X-ray crystallography; however, a XANES/EXAFS study has shown that it contains a short metal−oxo bond consistent with a triply bonded terminal oxo group, which gives rise to a pre-edge feature in the XANES spectrum. This feature has become a fingerprint for the presence of high-valent metal−oxo groups.

A detailed spectroelectrochemical study of both **1** and **2** has revealed multiple reversible redox processes for both compounds. Of particular interest is the relatively low potential for the $Mn^V \rightarrow Mn^{IV}$ process in **1** (near 0.0 V vs SCE), which shows that the Mn^V−oxo complex is not as strong an oxidant as might be expected from the high Mn oxidation state. In addition, the putative Mn^{IV}−oxo product species should be much less stable than a Mn^V−oxo species on the basis of electronic grounds (a d^3 vs d^2 metal−oxo), and this prediction is borne out by the data, which indicate that the product of the reduction near 0.0 V is extremely

(56) Groves, J. T.; Stern, M. K. *J. Am. Chem. Soc.* **1988**, *110*, 8628−8638.
(57) Camenzind, M. J.; Hollander, F. J.; Hill, C. L. *Inorg. Chem.* **1983**, *22*, 3776−3784.
(58) Connelly, N. G.; Geiger, W. E. *Chem. Rev.* **1996**, *96*, 877−910.
(59) Hureau, C.; Anxolabehere-Mallart, E.; Nierlich, M.; Gonnet, F.; Riviere, E.; Blondin, G. *Eur. J. Inorg. Chem.* **2002**, 2710−2719.
(60) Cooper, S. R.; Dismukes, G. C.; Klein, M. P.; Calvin, M. *J. Am. Chem. Soc.* **1978**, *100*, 7248−7252.
(61) Hureau, C.; Blondin, G.; Cesario, M.; Un, S. *J. Am. Chem. Soc.* **2003**, *125*, 11637−11645.

unstable, undergoing a conversion to another species on the electrochemical time scale. Thus, isolation or characterization of the elusive Mn^{IV}−oxo species needs a special approach, perhaps through low-temperature methods. An unexpected finding was the easy conversion of the Mn^{III} complex to the Mn^{V}−oxo species in pyridine by electrooxidation. This result points to possible new synthetic/electrochemical methods for the bulk preparation of Mn^{V}−oxo and other high-valent metal−oxo corrolazine compounds.

Acknowledgment. The support of the NSF (CHE0094095 to D.P.G.), NIH (GM-45205 to J.E.P.H.), and the Robert A. Welch Foundation (Grant E−680, K.M.K.) is gratefully acknowledged. M.C. is grateful for financial support from The Foundation Blanceflor Boncompangi-Ludovisi, née Bildt and the Stiftelsen Längmanska Kulturfonden. XAS data were obtained at the National Synchrotron Light Source beam line X9B, which is supported by the NIH-RR program; NSLS is operated by the US Department of Energy. HFEPR experiments were performed at the National High Magnetic Field Laboratory, which is funded by the NSF through the Cooperative Agreement No. DMR-0084173 and the State of Florida. The 25-T resistive magnet was funded by the W. M. Keck Foundation.

Supporting Information Available: X-ray crystallographic file for compound **2**·(CH_3OH) (CIF); UV−vis spectra of the addition of methanol to **2** (Figure S1), time-resolved thin-layer UV−vis spectra for **2** (Figure S2) and **1** (Figure S4), and thin-layer cyclic voltammograms for **1** (Figure S3). This material is available free of charge via the Internet at http://pubs.acs.org.

IC0503636